Journal of the Korean Astronomical Society
49: 9 ∼ 18, 2016 February

http://dx.doi.org/10.5303/JKAS.2016.49.1.9
pISSN: 1225-4614 · eISSN: 2288-890X
http://jkas.kas.org

Euclid Asteroseismology and Kuiper Belt Objects

Andrew Gould[1], Daniel Huber[2,3,4], and Dennis Stello[2,4]

[1]Department of Astronomy Ohio State University, 140 W. 18th Ave., Columbus, OH 43210, USA
gould@astronomy.ohio-state.edu
[2]School of Physics, University of Sydney, NSW 2006, Australia; dhuber,stello@physics.usyd.edu.au
[3]SETI Institute, 189 Bernardo Avenue, Mountain View, CA 94043, USA
[4]Stellar Astrophysics Centre, Department of Physics and Astronomy, Aarhus University, Ny Munkegade 120, DK-8000 Aarhus C, Denmark

Received April 27, 2015; accepted December 20, 2015

Abstract: *Euclid*, which is primarily a dark-energy/cosmology mission, may have a microlensing component, consisting of perhaps four dedicated one-month campaigns aimed at the Galactic bulge. We show that such a program would yield excellent auxilliary science, including asteroseismology detections for about 100 000 giant stars, and detection of about 1000 Kuiper Belt Objects (KBOs), down to 2–2.5 mag below the observed break in the KBO luminosity function at $I \sim 26$. For the 400 KBOs below the break, *Euclid* will measure accurate orbits, with fractional period errors $\lesssim 2.5\%$.

Key words: astrometry — gravitational microlensing — stars: oscillations — Kuiper belt

1. Introduction

In two earlier papers, we pointed out that *WFIRST* microlensing observations toward the Galactic bulge would automatically yield a treasure trove of asteroseismic (Gould et al. 2015) and Kuiper Belt Object (KBO) (Gould 2014) data. These papers contained detailed analytic calculations that permit relatively easy scaling to other missions and experiments. One very relevant mission is *Euclid*, which is presently scheduled to be launched in 2020. Unlike *WFIRST*, *Euclid* does not yet have a microlensing component, but such a component is being actively discussed.

Based on a most naive assessment, *Euclid* would appear to be much less effective in extracting non-microlensing science from microlensing data than *WFIRST*. *Euclid* has 1/2 the telescope diameter of *WFIRST*, 2.7 times larger linear pixel scale, 1/4 as many visits to each target, and 1/2 the angular area of the survey.

However, as we show, such naive assessment would be quite wrong since *Euclid* will be able to detect oscillations in giants that are about 0.8 mag brighter than for *WFIRST*, i.e., to about 0.8 mag above the red clump. Hence, it will obtain asteroseismic measurements for roughly 100 000 stars.

For KBOs, *Euclid* benefits by having an optical channel in addition to its primary infrared (IR) channel, even though it is expected that the optical exposure time will be 3 times smaller than for the IR. The optical observations gain substantially from their smaller point spread function (PSF) as well as the fact that KBOs (unlike stars) do not suffer extinction. Hence, *Euclid* will also be a powerful probe of KBOs.

Corresponding author: A. Gould

2. Euclid Characteristics

We adopt *Euclid* survey characteristics from Penny et al. (2013), with some slight (and specified) variations. In each case, for easy reference, we place the corresponding assumed *WFIRST* parameters in parentheses. Mirror diameter $D = 1.2\,\mathrm{m}$ (2.4 m); pixel size $p = 0.3''$ ($0.11''$), detector size 8k×8k (16k×16k), median wavelength $\lambda = 1.7\,\mu\mathrm{m}$ ($1.5\,\mu\mathrm{m}$), photometric zero point $H_{\rm vega} = 23.5$ (26.1), exposure time 52s (52s), effective background (including read noise, $H_{\rm vega,sky} = 20.0\,\mathrm{arcsec}^{-2}$, and dark current) $209\,e^-$ ($341\,e^-$), full pixel well $n_{\rm max} = 10^5$ (10^5), and single read time $t_{\rm single} = 2.6\,\mathrm{s}$ ($t_{\rm single} = 2.6\,\mathrm{s}$). In fact, Penny et al. (2013) do not specify a read time, so we use the same value as for *WFIRST* to simplify the comparison. Also, Penny et al. (2013) adopt an exposure time of 54 s, but we use 52 to again simplify the comparison. Finally, Penny et al. (2013) list $n_{\rm max} = 2^{16}$, but this appears to be in error. In any case, since the detector is very similar to *WFIRST*, these two numbers should be the same.

The most striking of these differences is the 2.6 mag (factor 11) difference in zero points because only a factor 4 is accounted for by the difference in mirror sizes. The two other principal factors are shorter bandpass (1.4–2.0 μm vs. 1.0–2.0 μm) and lower peak throughput (47% vs. 77%), with the latter primarily due to the fact that *Euclid* employs a dichroic beamsplitter whereas *WFIRST* does not, and (very secondarily) *WFIRST* has IR-optimized gold mirrors, which *Euclid* does not.

In our calculations we first consider simple 52 s exposures, but later take account of the fact that five such exposures will be carried out in sequence over $\sim 285\,\mathrm{s}$.

3. ASTEROSEISMOLOGY

3.1. Bright-Star Photometry

From Equation (16) of Gould et al. (2015), the fractional error (statistical) in the log flux F (essentially, magnitude error) is

$$\sigma(\ln F) = [\pi n_{\rm max}(3-Q)]^{-1/2} r_{\rm unsat}^{-1}; \quad r_{\rm unsat} \equiv \frac{\theta_{\rm unsat}}{p} \tag{1}$$

where p is the pixel size, $\theta_{\rm unsat}$ is the radius of the closest unsaturated pixel (in the full read), $n_{\rm max}$ is the full well of the pixel,

$$Q = N_{\rm read}^{-1} + 3(2N_{\rm read})^{-2/3}, \tag{2}$$

and $N_{\rm read}$ is the number of non-destructive reads.

When comparing *WFIRST* and *Euclid*, the most important factor is $r_{\rm unsat}$. To determine how this scales with mirror size, pixel size, exposure time t, throughput f, and mean wavelength λ, we adopt a common PSF function of angle θ, $A(D\theta/\lambda)$, which is scaled such that $\int dx 2\pi x A(x) \equiv 1$. Then, if a total of K photons fall on the telescope aperture, the number falling in a pixel centered at θ is

$$n_{\rm pixel} = p^2 K f A(D\theta/\lambda)(D/\lambda)^2 \tag{3}$$

Setting $n_{\rm pixel} = n_{\rm max}$, we derive

$$r_{\rm unsat} = \frac{A^{-1}[n_{\rm max}\lambda^2/(KfD^2p^2)]}{pD/\lambda}. \tag{4}$$

Then noting that $K = kfN_{\rm read}t_{\rm single}D^2$, where k is a constant, we obtain

$$r_{\rm unsat} = \frac{A^{-1}[n_{\rm max}\lambda^2/(kft_{\rm single}N_{\rm read}D^4p^2)]}{pD/\lambda} \tag{5}$$

Finally, noting that in the relevant range, a broad-band Airy profile scales $A(x) \propto x^{-3}$, we find a ratio of *Euclid* (E) to *WFIRST* (W) unsaturated radii,

$$\frac{r_{{\rm unsat},E}}{r_{{\rm unsat},W}} = \left[\frac{(N_{\rm read}D\lambda f/p)_E}{(N_{\rm read}D\lambda f/p)_W}\right]^{1/3} \simeq 0.42. \tag{6}$$

In making this evaluation we note that $(D_E/D_W) = 0.50$, $(p_E/p_W) = 2.73$, $(\lambda_E/\lambda_W) = 1.13$, and $(f_E/f_W) = 10^{0.4(23.52-26.1)}/(D_E/D_W)^2 = 0.365$. The last number may be somewhat surprising. It derives mainly from *WFIRST*'s broader passband (1 μm vs. 0.6 μm and its gold-plated (so infrared optimized) mirror. The other ratio of factors is

$$\frac{3-Q_E}{3-Q_W} = 1. \tag{7}$$

Therefore, we conclude that in the regime that the central pixel is saturated in a single read, a sequence of 5 *Euclid* exposures (requiring about 285 s including readout) yields a factor 1.06 increase in photometric errors compared to a single *WFIRST* exposure (lasting 52 s).

However, whereas this regime applies to stars $H < 11.6$ for *WFIRST* (x-intercept of lower curve of middle panel in Figure 1 of Gould et al. 2015), this break occurs at a brighter value for *Euclid*. To evaluate this offset, we rewrite Equation (3): $N_{\rm pixel} = kfN_{\rm read}t_{\rm single}(D^2p/\lambda)^2A(rDp/\lambda)$. Hence, the offset (at fixed r) between the break points on the *WFIRST* and *Euclid* diagrams is

$$\Delta H = -2.5\log[fD\lambda/p]_E/[fD\lambda/p]_H = 2.8 \tag{8}$$

That is, this boundary occurs at $H = 11.6 - \Delta H = 8.8$, which is significantly brighter than the majority of potential asteroseismic targets. However, inspection of that Figure shows that the same scaling ($\sigma \propto F_H^{-1/3}$) applies on both sides of the $H = 11.6$ "boundary". The reason for this is quite simple. As we consider fainter source stars F_H, the saturated region of course continues to decline. Since the Airy profile at large radii scales as $A(x) \propto x^{-3}$, the radius of this region scales as $r_{\rm unsat} \propto F_H^{1/3}$. Hence, the number of semi-saturated pixels (each contributing $n_{\rm max}$ to the total photon counts) scales $\propto F_H^{2/3}$, which implies that the fractional error scales $\propto F_H^{-1/3}$. This breaks down only at (or actually, close to) the point that the central pixel is unsaturated in a full read (at which point the error assumes standard $\propto F_H^{-1/2}$ scaling). That is, in the case of *Euclid*, the $F_H^{-1/3}$ scaling applies to about $H < 14.8 - \Delta H = 12.0$, which is still toward the bright end of potential targets.

3.2. Bright-Star Astrometry

From Gould et al. (2015)

$$\sigma(\theta) = \frac{p}{\sqrt{3\pi n_{\rm max}\ln(1.78N_{\rm read}+0.9)}}, \tag{9}$$

in the saturated regime. Hence, using the same parameters (for a single *Euclid* sub-exposure)

$$\frac{\sigma(\theta)_E}{\sigma(\theta)_W} = 2.73. \tag{10}$$

Then taking account of the fact that *Euclid* has five such sub-exposures, we obtain $\sigma(\theta)_E/\sigma(\theta)_W = 1.22$, i.e., *Euclid* is very similar to *WFIRST*.

However, as in the case of photometric errors, the boundary of the regime to which this applies is $H < 8.8$ for *Euclid* (compared to $H < 11.6$ for *WFIRST*). And, more importantly, for astrometric errors, the functional form of errors does in fact change beyond this break (see Figure 1 of Gould et al. 2015).

The reason for this change in form of astrometric errors can be understood by essentially the same argument given for the form of photometric errors in the previous section. In the regime between saturation of the central pixel in one read and $N_{\rm read}$ reads, the region $r < r_{\rm unsat} \propto F_H^{1/3}$ dominates the astrometric signal. For astrometric signals, each pixel contributes to

Table 1
Fundamental properties and simulation parameters for *Euclid* simulations.

Parameter	2437965	2425631	2836038
$T_{\rm eff}$ (K)	4356	4568	4775
$\log g$ (cgs)	1.765	2.207	2.460
[Fe/H] (dex)	0.43	−0.10	0.33
$R(R_\odot)$	24.94	16.44	11.28
M_H (mag)	−3.14	−2.38	−1.60
A_H/A_{Kp}	0.45	0.45	0.45
σ_E (mmag)	0.483	0.685	0.984
Reference	P14	P14	C14

Numbers in the first line are KIC IDs. References: P14 = Pinsonneault et al. (2014); C14 = Casagrande et al. (2014).

the $(\mathrm{S/N})^2$ as $n_{\rm max}/r^2$, and therefore the entire region contributes

$$\left(\frac{\mathrm{S}}{\mathrm{N}}\right)^2 \propto \int_1^{r_{\rm unsat}} \frac{rdr}{r^2} = \ln r_{\rm unsat};\ r_{\rm unsat} \propto F_H^{1/3} \quad (11)$$

Hence, between these two limits ($11.6 < H < 14.8$ for *WFIRST* and $8.8 < H < 12$ for *Euclid*) the astrometric errors should scale $\sigma \propto (\ln F^{1/3})^{-1/2} \propto (\ln F)^{-1/2}$. That is, these errors should increase by a factor $\sqrt{\ln N_{\rm read}} = 1.73$, which is indeed very similar to what is seen in Figure 1 of Gould et al. 2015.

3.3. Analytic Error Estimates for Bright Euclid Stars

We summarize the results of Sections 3.1 and 3.2 in the form of analytic expressions for the photometric and astrometric errors for bright stars as a function of magnitude for single-epoch *Euclid* observations consisting of 5 52-second exposures. The photometric errors are,

$$\begin{aligned} \sigma_{\rm phot} &= 0.47\,{\rm mmag}\,10^{(2/15)(H-12)},\ (H<12) \\ \sigma_{\rm phot} &= 0.47\,{\rm mmag}\,10^{(1/5)(H-12)},\ (H>12) \end{aligned} \quad (12)$$

The astrometric errors are

$$\begin{aligned} \sigma_{\rm ast} &= 73\,\mu{\rm as} \quad (4.4<H<8.8) \\ \sigma_{\rm ast} &= 73\,\mu{\rm as}\sqrt{\frac{\ln 10}{2.5}(H-8.8)+1} \quad (8.8<H<12) \\ \sigma_{\rm ast} &= 145\,\mu{\rm as}\,10^{(1/5)(H-12)} \quad (H>12) \end{aligned} \quad (13)$$

3.4. Asteroseismic Simulations for Euclid

As for *WFIRST*, we evaluate the asteroseismic capabilities of *Euclid* by its ability to recover the frequency of maximum power $\nu_{\rm max}$ and the large frequency separation $\Delta\nu$. Both are key quantities that can be used to estimate radii and masses for large ensembles of giants, as demonstrated with the *Kepler* sample (e.g., Kallinger et al. 2010; Hekker et al. 2011; Mosser et al. 2012).

Figures 1, 2, are the *Euclid* analogs of Figures 3, and 4 from Gould et al. (2015) for *WFIRST*, while Figure 3 illustrates the same physics as Figure 5 from Gould et al. (2015). In addition to incorporating the analytic formulae summarized in Section 3.3, they also take account of the following assumptions about the *Euclid* microlensing observations. First, they assume an 18 minute observing cycle (compared to 15 minutes for *WFIRST*). Second, they assume four 30-day observing campaigns (compared to six 72-day campaigns for *WFIRST*). Finally, we adopt a specific "on-off" (bold, normal) schedule of (**30**,124,**30**,335,**30**,181,**30**) days. This schedule has been chosen to be consistent with the *Euclid* sun-exclusion angle and to have two campaigns in each of the spring and autumn (useful for parallaxes) but is otherwise arbitrary.

The area under the spectral window function in Figure 1 is about 2.4 times larger than for *WFIRST* due to the fact that the campaigns are a factor $72/30 = 2.4$ times shorter. Nevertheless, the FWHM of this envelope is still only about 500 nHz, which is far less than the $\nu_{\rm max} \sim 8\,\mu$Hz for the brightest star shown in Figure 2. Hence, it is only for extremely bright stars that the width of this envelope will degrade the measurement of $\nu_{\rm max}$.

Figure 2 is qualitatively similar to Figure 4 from Gould et al. (2015). Note that as for the *WFIRST* simulations, the *Kepler* time series has been shorted to the assumed full duration (with gaps, 760 days) of the *Euclid* run to allow a direct comparison of the effects of sampling. As shown in Sections 3.1 and 3.3, the individual photometric measurements have very similar precision for *WFIRST* and *Euclid* in the relevant magnitude range. However, *Euclid* has a factor $(18/15) \times (72/30) \times (6/4) = 4.0$ times fewer of them, which leads to a factor 2.0 less sensitivity. This means that the "noise floor" kicks in at a power density of about $10^{3.3}\,{\rm ppm}^2\,\mu{\rm Hz}^{-1}$ rather than $10^{3.0}$. This is the reason that in the bottom panel, the $\nu_{\rm max}$ peak is not visible above the floor, whereas for *WFIRST* it is robustly visible (middle panel of Figure 4 of Gould et al. 2015). On the other hand, the $\nu_{\rm max}$ peak in the top panel is about equally robust in simulated *WFIRST* and *Euclid* data. The middle panel represents the approximate limit of *Euclid*'s ability to measure $\nu_{\rm max}$.

Figure 3 is an échelle diagram for the spectrum shown in the middle panel of Figure 2, i.e., the one just described that is at the limit of *Euclid*'s ability to measure $\nu_{\rm max}$. Figure 3 shows that this star is also just above the limit of *Euclid*'s ability to measure the other key asteroseismic parameter, the large frequency spacing $\Delta\nu$. In these diagrams, the abscissa designates frequency modulo the adopted $\Delta\nu$, while the ordinate is frequency. Hence, they represent the power spectrum divided into $\Delta\nu$-wide bins and stacked one above the other. If the adopted $\Delta\nu$ is correct (and the data are of sufficient quality) then the diagram should look like a series of vertical streaks, one for each mode degree ($l = 1, 2, 0$) comprising a series of overtones. This is clearly the case for the original *Kepler* data. While the ridges in the simulated Euclid data are heavily smeared out due to the window function, an identification of the correct $\Delta\nu$ is still possible. Hence both $\nu_{\rm max}$ and $\Delta\nu$ are measurable for this star. These quantities should also be measurable for brighter giants because these have both

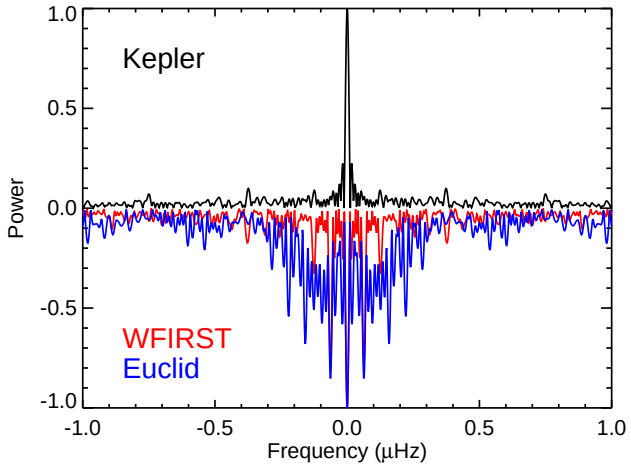

Figure 1. Spectral window function for a typical *Kepler* time series (top panel, black) and after degrading the time series to a typical duty cycle expected for *Euclid* and *WFIRST* (bottom panel, blue, red). Note that while the *Euclid* peak is much broader than for *Kepler* the power is still contained within $\sim 0.5\,\mu$Hz, which is substantially narrower than most spectral features of interest for most stars.

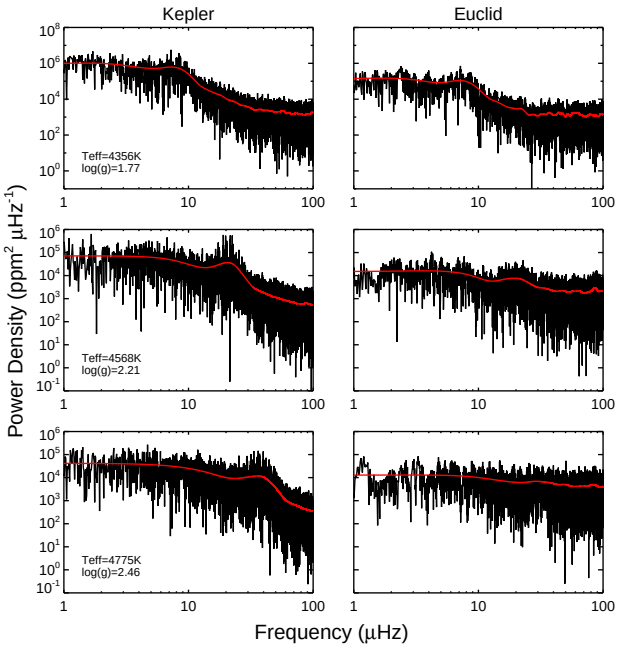

Figure 2. Power spectra of *Kepler* observations (left panels) and simulated *Euclid* observations (right panels) for three red giants in different evolutionary stages: high-luminosity red giant (top panels), 0.8 mag above red clump (middle panels) and red clump star (bottom panels). Red lines show the power spectra smoothed with a Gaussian with a full-width half-maximum of $2\Delta\nu$. Estimated stellar properties are given in the left panels, with a more complete description given in Table 1.

larger amplitude oscillations and smaller photometric errors, although for the most luminous giants the frequency resolution for a typical *Euclid* observing run will be too low to resolve $\Delta\nu$.

3.5. Role of Euclid Parallaxes

In Gould et al. (2015), we argued that *WFIRST* parallaxes could help resolve ambiguities in the measurement of $\Delta\nu$ due to aliasing. That is, from color-surface brightness relations, one approximately knows the angular radius, which combined with the measured parallax, gives the physical radius R. By combining R, $\nu_{\rm max}$, and general scaling relations, one can approximately predict $\Delta\nu$, and so determine which of the alias-peaks should be centroided to find a more precise value.

However, this does not work for *Euclid*. From Equation (13) and the fact that there are a total of $\sim 10\,000$ observations, it follows that the parallax errors are

$$\begin{aligned}\sigma(\pi) &= 8\,\mu{\rm as}\sqrt{\frac{\ln 10}{2.5}(H-8.8)+1} \quad (8.8<H<12)\\ \sigma(\pi) &= 15\,\mu{\rm as}\,10^{(1/5)(H-12)} \quad (H>12) \qquad (14)\end{aligned}$$

Hence, at the brightness of targets near the boundary of measurability, $H\sim 13$, the parallax errors are roughly 20%, which provides essentially no information. Even for the rarer targets at $H\sim 12$, the parallax measurements do little more than confirm that the star is in the bulge, which is already basically known in most cases. Nevertheless, these parallaxes are substantially better than Gaia parallaxes for the same stars and so could be useful for other purposes.

4. KUIPER BELT OBJECTS

Gould (2014) carried out analytic calculations to assess how well *WFIRST* could detect and characterize Kuiper Belt Objects (KBOs), including orbits, binarity, and radii. He employed a Cartesian parameterization, first introduced by Bernstein & Khushalani (2000) to facilitate numerical calculations and KBO recovery from followup observations, and then further developed by Gould & Yee (2013) to facilitate analytic estimates of survey properties and their resulting measurements.

Here we apply these analytic formulae to *Euclid*.

In contrast to *WFIRST*, *Euclid* will observe in two channels simultaneously, using an optical/IR dichroic beam-splitter. Because the microlensing targets will be heavily extincted in the optical, and also because bandwidth considerations restrict the optical downloads to once per hour (vs. once per 18 minutes for the IR), the optical data will provide only supplementary information for microlensing events. Similarly, for the heavily reddened (and intrinsically red) asteroseismology targets, the optical images will also be of secondary importance, and so were not considered in Section 3. However, KBOs lie in front of all the dust and hence both the optical and IR channels should be considered.

4.1. Euclid IR Observations of KBOs

We remind the reader that, in contrast to asteroseismology targets, KBOs are below the sky level and therefore are in a completely different scaling regime. In order to make use of the analytic formulae of Gould (2014), we

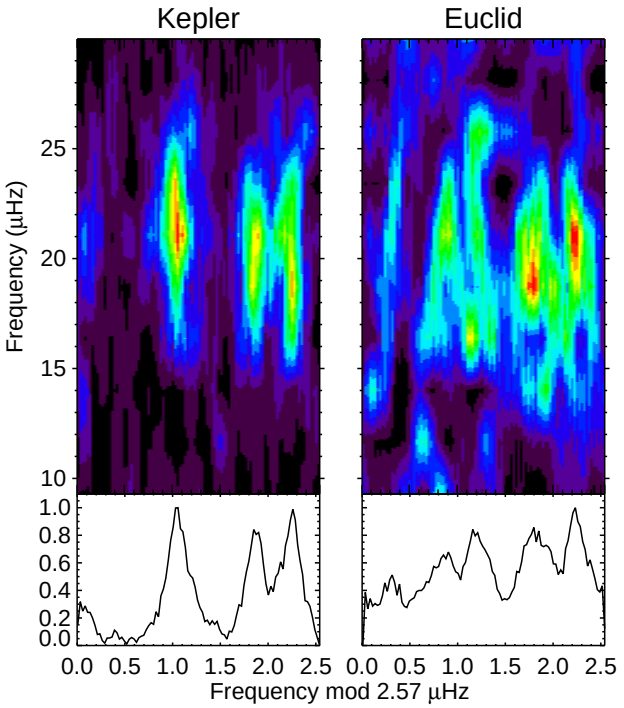

Figure 3. Échelle diagram for KIC 2425631 (corresponding to middle panel of Figure 2) for *Kepler* (left) and simulated *Euclid* (right) data. The abscissa is the frequency offset relative to the beginning of each order, which are separated by (an adopted) large-frequency spacing $\Delta\nu = 2.57\,\mu$Hz. Hence, for example, at the frequency of maximum power $\nu_{\rm max} \sim 20\,\mu$Hz, the ordinate corresponds to the eighth order. In the *Kepler* échelle, the three mode degrees $l = 1, 2, 0$ from left to right are easily discerned, which is not true of the *Euclid* échelle. However, the *Euclid* échelle does display clear vertical "streaking" which is the signature that the adopted $\Delta\nu = 2.57\,\mu$Hz is the correct one.

first note that the *Euclid* point spread function (PSF) is slightly more undersampled than that of *WFIRST* by a factor $(0.30/0.11) \times (1.2/2.4) \times (1.5/1.7) = 1.2$. We therefore adopt an effective sky background of $6B$, where $B = 209\,e^-$ is the effective background in a single pixel (compared to $3B$ for the oversampled limit). That is, $H_{\rm sky} = 23.5 - 2.5\log(6B/52) = 20$, i.e., 1.7 mag brighter than for *WFIRST*. Then, following Equation (3) of Gould (2014), we estimate the astrometric precision of each measurement as

$$\sigma_{\rm ast} = \sqrt{2}\frac{\sigma_{\rm psf}}{\rm SNR} = \frac{212\,{\rm mas}}{\rm SNR}, \qquad (15)$$

i.e., exactly twice the value for *WFIRST* (because the mirror is two times smaller). Here, the signal-to-noise ratio (SNR) of 5 co-added consecutive observations is given by

$${\rm SNR} = 10^{0.4(H_{\rm zero}-H)}, \qquad H_{\rm zero} = 24.8. \qquad (16)$$

Comparing this to Equation (1) of Gould (2014), we see that $H_{\rm zero}$ is 3.5 mag brighter than for *WFIRST*.

Before continuing, we remark on the issue of smeared images, which is potentially more severe for *Euclid* than *WFIRST* because the full duration of the 5 co-added exposures is about 5.5 times longer than the *WFIRST* exposure. However, due to the shorter duration of the observing window and the fact that this window has one end roughly at quadrature (and the other 30 days toward opposition), the typical relative velocities of the KBO and satellite are only about $5\,{\rm km\,s^{-1}}$, which corresponds to $\sim 10\,\mu{\rm as\,min^{-1}}$, which is still too small to substantially smear out the PSF, even in ~ 5 min exposures.

Although the area of the *Euclid* field is only about half the size of the *WFIRST* field, the fact that the campaign duration is only 40% as long together with the very slow mean relative motion of the KBOs (previous paragraph) implies that this is even less of an issue than for *WFIRST*, which Gould (2014) showed was already quite minor. We therefore ignore it.

As with *WFIRST*, we assume that only 90% of the observations are usable, due to contamination of the others by bright stars. This balances the opposite impact of two effects: larger pixels increase the chance that a given bright star lands on the central pixel, while brighter $H_{\rm zero}$ decreases the pool of bright stars that can contribute to contamination. We also assume that 10% of the observing time is spent on other bands. These will provide important color information but are difficult or impossible to integrate into initial detection algorithms. Hence the total number of epochs per campaign is $N_{\rm cam} = 1920$, i.e., a factor ~ 3 smaller than for *WFIRST*.

4.2. Correction to Gould (2014) Formula: Number of Trials

To determine the minimum total SNR required for a detection, we must determine the number of trials. In principle, we should be able to simply scale from Equation (18) of Gould (2014). However, this equation contains a significant error in the "radial velocity" term, which must be corrected. We then take this opportunity to rederive the entire formula in order to put it in more general form.

Our guiding assumption is that the predictions of a given trial must match the orbit of a KBO to within half a pixel for all epochs. There are six phase space coordinates, two for transverse position at the midpoint of observations, two for proper motion ($\boldsymbol{\mu}$) at this epoch, one for distance (r), and one for radial velocity (v_r), both at the same epoch.

The first (position) term implies $4A/\theta_{\rm pixel}^2$ initial positions, where $\theta_{\rm pixel}$ is the size of a pixel and A is the angular area of the region probed. The second (proper motion) term requires $\pi(\mu_{\rm max}\Delta t/\theta_{\rm pixel})^2$ trials for each position, where $\mu_{\rm max}$ is the maximum search radius (relative to a KBO on a circular orbit), and Δt is the duration of continuous observations.

For observations near quadrature, the accelerated motion of Earth causes a maximum displacement of $\Delta\theta = (1/2)(\Omega\Delta t/2)^2\Pi$ where $\Pi = {\rm AU}/r$ and $\Omega = {\rm yr}/2\pi$. Hence, a total of $2\Delta\theta/\theta_{\rm pixel} = (1/4)(\Omega\Delta t)^2\Delta\Pi/\theta_{\rm pixel}$ independent searches must be

conducted for each position/proper motion being considered. Here $\Delta\Pi$ is the range of parallaxes being probed. In principle, one must consider that this number may be less than one, in which case of course a minimum of unity must be imposed. In practice, however, for experiments with *WFIRST* and *Euclid*, this number easily exceeds unity.

Finally, to evaluate the v_r contribution, we should consider how two orbits differ in projection if they have identical $\boldsymbol{\theta}_0$, $\boldsymbol{\mu}_0$, and Π_0, but differ in Δv_r. This is just

$$\Delta\theta = \frac{\Delta v_r \Delta t/2}{r} \frac{(1/2)(\Omega\Delta t/2)^2 \mathrm{AU}}{r} = \frac{\Delta v_r \Omega^2 \mathrm{AU}}{16 r^2} (\Delta t)^3 \tag{17}$$

In contrast to the previous term, we actually do need to evaluate the conditions under which this term is greater than $\theta_{\rm pixel}/2$. That is, whether the predicted number of trials

$$\begin{aligned} N_{v_r} &= \frac{2\Delta\theta}{\theta_{\rm pixel}} = \frac{\Delta v_{r,\rm max} \Omega^2 \mathrm{AU}}{8 r^2 \theta_{\rm pixel}} (\Delta t)^3 \\ &= 37 \frac{\Delta v_{r,\rm max}}{4 \mathrm{km\,s^{-1}}} \left(\frac{\theta_{\rm pixel}}{110\,\mathrm{mas}} \right)^{-1} \\ &\quad \times \left(\frac{r}{40\,\mathrm{AU}} \right)^{-2} \left(\frac{\Delta t}{72\,\mathrm{days}} \right)^{3} \end{aligned} \tag{18}$$

is greater than unity. In Equation (18), we have normalized this calculation to *WFIRST* assumptions, in particular the $\Delta t = 72$ day campaigns. We have also adopted a full range of $\Delta v_r = 4\,\mathrm{km\,s^{-1}}$ (i.e., $\pm 2\,\mathrm{km\,s^{-1}}$) for the radial velocity search. Hence, there are two regimes

$$\begin{aligned} N_{\rm try,0} &= 4 \times 10^{13} \frac{A}{\mathrm{deg}^2} \left(\frac{\theta_{\rm pixel}}{110\,\mathrm{mas}} \right)^{-5} \left(\frac{\Delta\mu_{\rm max}}{12''/\mathrm{day}} \right)^{2} \\ &\quad \times \frac{\Delta\Pi}{1/40} \left(\frac{\Delta t}{\mathrm{day}} \right)^{4} \end{aligned} \tag{19}$$

or

$$N_{\rm try} = N_{\rm try,0} \times N_{v_r} \tag{20}$$

Before proceeding, we note that, by chance, Equation (20) is just a factor 2 larger than the result reported by Gould (2014) for *WFIRST* parameters. Since this is well below the uncertainty in the estimates of computational efficiency a decade from now, the results of that paper are essentially unchanged.

For *Euclid*, with its shorter ($\Delta t = 30$ day) campaigns and larger (300 mas) pixels, $N_{v_r} \simeq 1$. Hence, Equations (19) and (20) both yield the same result, $N_{\rm try} = 8 \times 10^{18}$. This is 5.6 orders of magnitude smaller than the corresponding number for *WFIRST*. Hence, the challenges posed by limitations of computing power that were discussed by Gould (2014) are at most marginally relevant for *Euclid*. Therefore, we ignore them here.

Then to find the limiting SNR at which a KBO can be detected, we solve Equation (17) from Gould (2014), i.e.,

$$\mathrm{SNR} \gtrsim N_{\rm cam}^{-1/2} \sqrt{2 \ln \frac{N_{\rm try}}{\mathrm{SNR}} - \ln N_{\rm cam}} = 0.21, \tag{21}$$

where $N_{\rm cam}$ is the number of observations during a single-season observing campaign. Hence, the limiting magnitude is $H \lesssim 26.5$.

4.3. Euclid Optical Observations of KBOs

To compare optical with IR observations, we first note that the field of view is the same, but with pixels that are smaller by a factor 3. This means that the optical data are nearly critically sampled (100 mas pixels and 180 mas FWHM). The "RIZ" band is centered in I band and has a flux zero point of $I_{\rm vega} = 25.1$. As noted above, band-width constraints limit the number of optical images that can be downloaded (in addition to the primary IR images) to one per hour (for each of the three fields).

Taking into account the read noise of $4.5\,e^-$, a sky background of $I = 21.0\,\mathrm{arcsec}^{-2}$, and the nearly critical sampling, we find the analog of Equation (16) to be

$$\mathrm{SNR} = 10^{0.4(I_{\rm zero} - I)}, \qquad I_{\rm zero} = 27.4 \tag{22}$$

for 270 s exposures. Even allowing for the fact that there are only 30% as many I-band observations and that the typical color of a KBO is $I - H \sim 1$, this still represents an improvement of $27.4 - 24.8 - 1 + 2.5\log(0.3) = 0.3$ magnitudes relative to H band. Thus, the I-band observations will overall provide more information than H band, and we will henceforth focus primarily on these. We note however that H band data will be quite useful, both to measure KBO colors and confirm marginal detections,

An important benchmark for understanding the relative sensitivity of *WFIRST* and *Euclid* is that at the KBO luminosity function break ($R = 26.5$, $I = 26.0$, $H = 25.1$), we have SNR$\sim$ 2.5 for *WFIRST* and SNR$\sim$ 3.6 for *Euclid*.

For fixed field size and Δt, (and taking account of the fact that $N_{v_r,\rm IR} \simeq 1$ the number of trials scales $N_{\rm try} \propto \theta_{\rm pix}^{-6}$, i.e., $N_{\rm try} \sim 10^{22}$, a factor $10^{2.9}$ higher for the optical than the IR. This implies that reaching the theoretical detection limit will require roughly $10^{25.6}$ floating point operations (FLOPs). While this is 3.7 orders of magnitude lower than *WFIRST*, it is not trivially achieved (Gould 2014). For the moment we evaluate the detection limit assuming that it can be achieved and then qualify this conclusion further below. Assuming that 10% of observations are lost to bright stars and then solving Equation (21) yields SNR$\gtrsim 0.39$, i.e., a detection limit of $I \lesssim 28.4$. Considering that the break in the KBO luminosity function is $R \sim 26.5$ and that typically $R - I \sim 0.45$, this is about 1.5 mag below the break. Hence, *Euclid* optical observations will be a powerful probe of KBOs.

4.4. Detections

The main characteristics of the *Euclid* optical KBO survey can now be evaluated by comparing to the results of Gould (2014). The total number detected up to the break (and also the total number detected per magnitude between the break and the faint cutoff) will

be $(4/6)/2.1 = 32\%$ smaller than for *WFIRST* (Figure 4 from Gould 2014) because there are 4 campaigns (rather than 6) and the survey area is a factor 2.1 times smaller.

Thus, there will be a total of 400 KBOs discovered that are brighter than the break and 530 per magnitude fainter than the break. In fact, this distribution is only known to be flat for about 1.5 mag. *Euclid* observations will reach about 2.4 mag below the break, provided that the computational challenges can be solved. However, as we discuss in Section 4.8, even if they cannot be solved, this will pull back the magnitude limit by only a few tenths.

Hence, *Euclid* will discover at least 800 KBOs down to the point that the KBO luminosity function is measured, and perhaps a few hundred beyond that.

4.5. Orbital Precision

To determine the precision of the orbit solutions, we first note that the PSF is almost exactly the same size (both mirror and observing wavelength are half as big). Hence, Equation (12) from Gould (2014) remains valid:

$$\begin{aligned}\frac{\sigma(v_r)}{v_\oplus\sqrt{\Pi}} &= \frac{3.8\times10^{-3}}{\rm SNR}\left(\frac{N}{5600}\right)^{-1/2}\left(\frac{\Delta t}{72{\rm d}}\right)^{-3}\left(\frac{r}{40\,{\rm AU}}\right)^{5/2}\\ &= \frac{0.15}{\rm SNR}\left(\frac{N}{650}\right)^{-1/2}\left(\frac{\Delta t}{30{\rm d}}\right)^{-3}\left(\frac{r}{40\,{\rm AU}}\right)^{5/2}. \qquad (23)\end{aligned}$$

Here v_r is the instantaneous KBO radial velocity, r is the KBO distance, $\Pi = {\rm AU}/r$, $v_\oplus$ is Earth's orbital velocity, and N is the number of contributing images. Gould (2014) argued that because v_r was by far the worst measured KBO Cartesian coordinate, all orbital-parameter errors would scale with this number, and in particular for the period P (his Equation 13),

$$\frac{\sigma(P)}{P} \simeq \frac{3v_r}{v_\oplus\Pi^{1/2}}\frac{\sigma(v_r)}{v_\oplus\Pi^{1/2}}. \qquad (24)$$

Hence, at fixed SNR (per observation), *Euclid* period errors are a factor 40 larger than for *WFIRST*. The primary reason for this is the factor 2.4 shorter observing campaign, which enters as the third power. In addition, there are about 7 times fewer observations, which enters as the square root. At the break ($I\sim26$), we have from Equation (22), SNR$\simeq$ 3.6. Following Gould (2014), we adopt $v_r \sim 0.2v_\oplus\Pi^{1/2}$, and derive $\sigma(P)/P \sim 2.5\%$. This means that orbital precisions for KBOs below the break will be good enough to determine orbital families, but in most cases not good enough to detect detailed subtle structures.

4.6. Binaries

Microlensing-style observations can detect KBOs through two distinct channels: resolved companions and unresolved companions detected from center-of-light motion Gould (2014).

For resolved companions, the situation for *Euclid* is essentially identical to *WFIRST*. That is, the resolution is the same, and gain in sensitivity from reduction in trials is nearly the same. Therefore, *Euclid* can detect binaries down to $I \lesssim 29.3$. Note that because of the relatively small number of trials, this limit is independent of whether the computational challenges to reaching the $I = 28.4$ detection limit can actually be achieved.

Once the companion is detected, its proper motion (relative to the primary) can be measured with a precision (Equation 21 of Gould 2014)

$$\sigma(\Delta\mu) = \sqrt{\frac{24}{N}}\frac{\sigma_{\rm ast}}{\Delta t} = \frac{250\,{\rm mas\,yr^{-1}}}{\rm SNR}, \qquad (25)$$

where $\sigma_{\rm ast} = 105\,{\rm mas}$ is the Gaussian width of the PSF. This is a factor ~ 7 larger error than for *WFIRST*. Considering that single-epoch SNR for *Euclid* is $3.6/2.5 = 1.44$ better than for *WFIRST*, Equation (22) of Gould (2014) becomes $\Delta\mu \sim 83({\rm SNR})^{1/2}\eta^{-1/2}$ where η represents the binary separation relative to the Hills-sphere radius. Therefore, a 3-sigma detection of the proper motion requires $\eta \lesssim ({\rm SNR}/4.3)^3$. Hence, for example, at the break, $\eta \lesssim 0.6$. Since for KBOs at the break (diameter $D\sim 50\,{\rm km}$), and for orbits with $a\sim 40\,{\rm AU}$, the Hills sphere is at roughly $7''$, this still leaves plenty of room for detections with proper motion measurements. Such measurement can be used to statistically constrain the masses of the KBOs. However, the main problem is that most observed KBO companions are at much closer separations, indeed too close to be resolved.

Gould (2014) therefore investigated how well these could be detected from center-of-light motion. This requires that the companion be separated by less than a pixel (otherwise not unresolved), the period be shorter than the duration of observations (otherwise center-of-light internal motion cannot be disentangled from center-of-mass motion around the Sun), and high-enough ($\gtrsim 7$ sigma) detection to distinguish from noise spikes.

From Equation (23) of Gould (2014) for such detection, we have

$${\rm SNR} \gtrsim 7\sqrt{\frac{2}{650}}\frac{p}{f_{\rm cl}\theta_c} \gtrsim 4.85\frac{p}{\theta_c}\left(\frac{f_{\rm cl}}{0.08}\right)^{-1}, \qquad (26)$$

where θ_c is the binary projected separation and f_{cl} is the ratio of center-of-light to binary motion, which has a broad peak $0.07 \lesssim f_{\rm cl} \lesssim 0.09$ (Gould 2014). This corresponds to $I < 25.6$, i.e., almost a half mag above the break.

The requirement that the period obey $P_c < \Delta t$ implies that $\eta = (a/{\rm AU})^{-1}(P_c/{\rm yr})^{2/3} = 0.0047$. Hence, imposing $\theta_c = p$ (maximum unresolved orbit) yields a KBO diameter $D = pD_\odot/\eta = 145\,{\rm km}$, corresponding to $I\sim 23.5$, i.e., 2.5 mag above the break.

These analytic estimates imply that detection of binaries from light-centroid motion is much more difficult than with *WFIRST*, a conclusion that is confirmed by

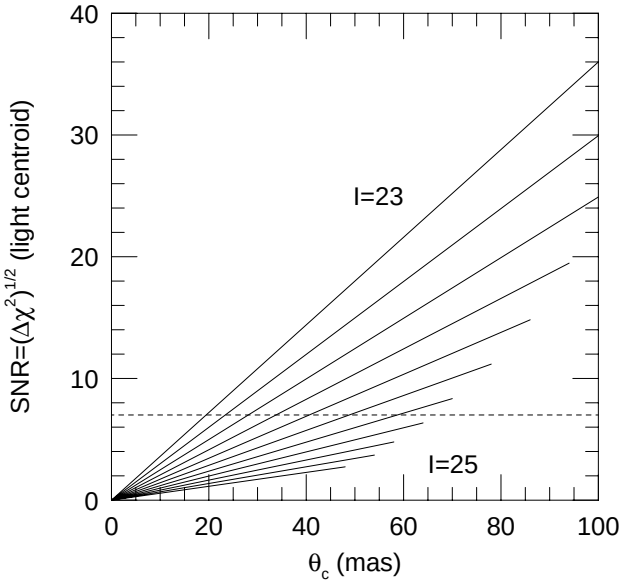

Figure 4. Signal-to-noise ratio $[(\Delta\chi^2)^{1/2}]$ for orbiting KBOs at a range of separations that are less than the *Euclid* optical pixel size $\theta_c < p = 100\,\mathrm{mas}$. The KBO brightness ranges from $I = 23$ to $I = 25$ as indicated. Tracks end to the right when the orbital period $P = \Delta t = 30\,\mathrm{days}$, the duration of an observing campaign. Longer period orbits would have substantially lower signal. The calculations assume $f_{\rm cl} = 8\%$ (see Figure 1 of Gould 2014). The region of partial (broad) sensitivity $I < 24$ ($I < 23$) will have only about 25 (6) detected KBOs, so not many binaries will be detected via this channel (in strong contrast to *WFIRST*.

Figure 4, which is the analog of Figure 2 from Gould (2014). It shows that such detections are impossible for $I > 24$ and begin to cover a wide range of separations only for $I < 23$. The total numbers of expected KBO detections in these ranges are ~ 25 and ~ 6, respectively. Hence, there will be very few binaries detected through the light-centroid channel.

4.7. Occultations

Similarly, *Euclid* will detect very few KBO occultations compared to the $\mathcal{O}(1000)$ occultations expected for *WFIRST*. First, the total number of (epochs)×(sky area) is smaller by a factor 27. Second, the exposure times are longer by a factor ~ 5. Since the occultations are typically shorter than the *WFIRST* exposure time, this means that the signal is ~ 5 times weaker for otherwise equivalent stars. This factor does also imply that the number of occultations is in principle larger by this same factor ~ 5 for similar trajectories, but having more occultations is of no help if they are each unobservably faint. Finally, because the fields are moderately extincted, the occulted stars are fainter in the I-band than in H. Therefore, we conclude that *Euclid* KBO occultations will not provide much information about KBOs.

4.8. Computational Challenges

As mentioned in Section 4.3, a total of $10^{25.6}$ FLOPs would be required to reach the detection limit of $I = 28.4$. By contrast, Gould (2014) argued that it would be straightforward today to carry out $10^{23.5}$ FLOPs per year, and that perhaps in 10 years Moore's Law might raise this number to 10^{25}. This would leave a shortfall of $q = 10^{2.1}$ or $q = 10^{0.6}$, in the two cases, respectively. If these shortfalls could not be overcome, then according to the argument given in Section 6 of Gould (2014), this would lead to a cutback of the magnitude limit by $\Delta I \sim (1.25/(n+1)\log q$, where $n = 4$ or $n = 7$ according to whether Equation (19) or Equation (20) from Section 4.2, above, is used. Since for *Euclid* optical observations $n = 7$ (Section 4.3), we have 0.3 or 0.1 mag in the two cases, respectively. Note that in both cases, the limit would still be beyond the current limit where the luminosity function is measured (i.e., 1.5 mag beyond the break). Hence, even if such computational challenges cannot be overcome, this will not compromise *Euclid*'s capability to explore new regimes of KBO parameter space.

4.9. Comparison to the Deep *HST* Search

It is of interest to compare the corrected formulae presented here with the practical experience of Bernstein et al. (2004), who searched for KBOs based on $N_{\rm cam} = 95$ *Hubble Space Telescope (HST)* epochs taken over $\Delta t = 15\,\mathrm{days}$ near quadrature, with a field size $A = 0.019\,\mathrm{deg}^2$ and pixel scale $\theta_{\rm pixel} = 50\,\mathrm{mas}$. They searched current distances $25\,\mathrm{AU} < r < \infty$, implying $\Delta\Pi = 0.04$, looking for all bound orbits with inclinations $i < 45°$, which roughly corresponds to $\Delta\mu = 15''/\mathrm{day}$ at a typical distance of $a \sim 40\,\mathrm{AU}$, and with perihelia $> 10\,\mathrm{AU}$, which corresponds to $-7\,\mathrm{km\,s^{-1}} < v_r < 7\,\mathrm{km\,s^{-1}}$, i.e., $\Delta v_r = 14\,\mathrm{km\,s^{-1}}$.

However, in contrast to the approximately uniform cadence anticipated for *WFIRST* and *Euclid*, the *HST* observations were grouped in two intervals of 5 days (55 exposures) and 4 days (40 exposures), separated by about 6 days. The two groups are labeled "discovery" and "recovery", respectively. For faint targets (of relevance here), the initial search is carried out on the discovery epoch, not the combination of the two.

They searched over only five (out of six) phase space coordinates because the "line-of-sight motion [r] has negligible observable effect over the course of the 15 day *HST* observation", This statement would only be marginally correct for the full observation sequence: Equation (18) would yield $N_{v_r} = 2.4$ for $r = 40\,\mathrm{AU}$ and $\Delta v_f = 14\,\mathrm{km\,s^{-1}}$. However, when considering only the first epoch (in accord with their actually procedures), it is strictly correct: $N_{v_r} = 0.1$.

Bernstein et al. (2004) state that for their search, $N_{\rm try} \propto \theta_{\rm pixel}^{-5}(\Delta t)^3$, which compares to the scaling $N_{\rm try} \propto \theta_{\rm pixel}^{-5}(\Delta t)^4$ shown in Equation (19). They do not give explicit reasoning for this scaling, but from context this conclusion seems to follow from the fact that three first derivatives enter their formalism (two

transverse positions and distance). However, as discussed in Section 4.2, linear changes in Earth's distance from the KBO (assumed not moving) lead to quadratic changes in Earth's transverse position. Even though this quadratic displacement can be described with a single parameter, it is the actual pixel displacement that matters in determining the number of trials. However, this scaling relation does not appear to have directly entered into their calculations, since they only carried this out with a single value of Δt.

According to Equation (19), there should have been $N_{\rm try} = 6 \times 10^{16}$ trials for the $\Delta t = 5\,$day discovery period. Bernstein et al. (2004) report that they searched a grid of 13 harmonically spaced distances r and a "total of 7.5×10^5 velocity grid points". Since in this search, they are using a 30 mas grid, there are 2.7×10^8 pixel positions, which implies $N_{\rm try} \sim 2 \times 10^{14}$, which is smaller by a factor ~ 300 than the value given by Equation (19).

The 13 distance grid points correspond to steps $\delta\Pi = (1/25)/(13-1) = 1/300$. The difference in final pixel positions between neighboring grid points is $(1/8)(\Omega\Delta t)^2\delta\Pi = 0.6''$, which is a factor 20 larger than the spatial grid sampling.

If we adopt the $5\,{\rm km\,s^{-1}}$ velocity radius estimated above at a "typical" distance of $r = 40\,$AU and assume that this distance grid point has 1/13 of the total velocity grid points, i.e., 6×10^4, then the grid spacing is $\delta v_\perp = 0.035\,{\rm km\,s^{-1}}$. This corresponds to an angular displacement of $\delta v_\perp(\Delta t/2)/r = 0.2''$, which is a factor 7 larger than the spatial sampling. Together, these two effects approximately account for the difference in estimates of $N_{\rm try}$.

What is the impact of this apparently too-sparse grid? If we assume that a half-pixel spacing is overly conservative, and that loss of information really only sets in at 1-pixel (for *HST* data), then combined information from multiple epochs only accumulates for $\Delta t/\sqrt{10}$ and $\Delta t/3.5$ for the parallax and for the proper motion, respectively, which both correspond to $\sim 1.5\,$days. This implies a loss of depth of $\Delta R = 1.25\log(5/1.5) \sim 0.65$ relative to what would be possible from the full 5-day discovery observations and 0.95 mag relative to the full data set.

As in our discussion of future analyses of *Euclid* and *WFIRST* data, the cost of fairly dramatic reduction of computations is therefore relatively modest in terms of magnitude limit. And, as we have remarked, once the KBO has been discovered, the full data set can be used to confirm it and measure its orbital parameters.

5. CONCLUSION

We have applied to the *Euclid* mission analytic formulae that were previously derived for *WFIRST* in order to assess the implications of microlensing observations for asteroseismology and KBO science. In contrast to *WFIRST*, *Euclid* does not at present have a dedicated microlensing component. We have therefore used the survey parameters presented by Penny et al. (2013) as a guideline to a microlensing program that is being actively considered.

We find that for asteroseismology, *Euclid* observations are nearly as good as *WFIRST* on a star-by-star bases, although there are only half as many stars (due to half as much viewing area). This is somewhat surprising because of *Euclid*'s 4 times smaller aperture, 2.7 times lower throughput, and 4 times fewer epochs. However, these factors are partially compensated by having 5 times longer exposures. In addition, having a larger PSF is actual helpful, since fewer photons wind up in saturated pixels. In the end, however, the *Euclid* limit is about 0.8 mag brighter than for *WFIRST*, but this still implies that it will obtain excellent asteroseismology on about 100 000 stars.

We find that it is *Euclid*'s optical images that provide the best information about KBOs. These observations are auxiliary for the primary microlensing program because there are fewer of them and the stars are significantly extincted in the I band. The main microlensing use is to provide colors, which are important in the interpretation of the events. However, they are especially useful for KBO observations, first because KBOs (unlike stars) are not extincted, and second because the smaller PSF (and pixels) reduces the background and improves the astrometry.

We find that *Euclid* will detect about 400 KBOs below the break and about 530 per magnitude above the break, down to about $I = 27.9$–28.4 (depending on whether the computational challenges can be solved). At the break, the periods (and other orbital parameters) will be measured to $\sim 2.5\%$. At other magnitudes, the errors scale inversely with flux. *Euclid* will be roughly equally sensitive (compared to *WFIRST*) to resolved binary companions, going down to about $I = 29.3$. However, in contrast to *WFIRST*, it will not detect many unresolved binaries via center-of-light motion.

ACKNOWLEDGMENTS

Work by AG was supported by NSF grant AST 1103471 and NASA grant NNX12AB99G. DH acknowledges support by the Australian Research Council's Discovery Projects funding scheme (project number DE140101364) and support by NASA under Grant NNX14AB92G issued through the Kepler Participating Scientist Program. We thank Matthew Penny for seminal discussions. This research was greatly facilitated by the interactive environment at the Galactic Archaeology Workshop at the Kavli Institute for Theoretical Physics in Santa Barbara.

REFERENCES

Bernstein. G. M., & Khushalani, B. 2000, Orbit Fitting and Uncertainties for Kuiper Belt Objects, AJ, 120, 3323

Bernstein. G. M., Trilling, D. E., Allen, R. L., et al. 2004, The Size Distribution of Trans-Neptunian Bodies, AJ, 128, 1364

Casagrande, L., Silva, A. V., Stello, D., et al. 2014, Strömgren Survey for Asteroseismology and Galactic Archaeology: Let the SAGA Begin, ApJ, 787, 110

Gould, A. 2015, WFIRST Ultra-Precise Astrometry I: Kuiper Belt Objects, JKAS, 48, 93
Gould, A., & Yee, J. C. 2013, Microlens Surveys are a Powerful Probe of Asteroids, ApJ, 767, 42
Gould, A., Huber, D., Penny, M., & Stello, D. 2015 WFIRST Ultra-Precise Astrometry II: Asteroseismology JKAS, 47, 279
Hekker, S., Elsworth, Y., De Ridder, J., et al. 2011, Solar-Like Oscillations in Red Giants Observed with Kepler: Comparison of Global Oscillation Parameters from Different Methods, A&A, 525A, 131
Kallinger, T., Weiss, W. W., Barban, C., et al. 2010, Oscillating Red Giants in the CoRoT Exofield: Asteroseismic Mass and Radius Determination, A&A, 509A, 77
Mosser, B., Elsworth, Y., Hekker, S., et al. 2011, Characterization of the Power Excess of Solar-Like Oscillations in Red Giants with Kepler, A&A, 537A, 30
Pinsonneault, M. P., Elsworth, Y., Epstein, C., et al. 2014, The APOKASC Catalog: An Asteroseismic and Spectroscopic Joint Survey of Targets in the Kepler Fields, ApJS, 215, 19
Penny, M. T., Kerins, E., Rattenbury, N., et al. 2013, ExELS: An Exoplanet Legacy Science Proposal for the ESA Euclid Mission I. Cold Exoplanets, MNRAS, 434, 2